
 **DOVE: Learning Deformable 3D Objects by Watching Videos**

Shangzhe Wu* Tomas Jakob* Christian Rupprecht Andrea Vedaldi

Visual Geometry Group, University of Oxford
{szwu, tomj, chrisr, vedaldi}@robots.ox.ac.uk

[dove3d.github.io](https://github.com/dove3d)

Abstract

Learning deformable 3D objects from 2D images is an extremely ill-posed problem. Existing methods rely on explicit supervision to establish multi-view correspondences, such as template shape models and keypoint annotations, which restricts their applicability on objects “in the wild”. In this paper, we propose to use monocular videos, which naturally provide correspondences across time, allowing us to learn 3D shapes of deformable object categories without explicit keypoints or template shapes. Specifically, we present *DOVE*, which learns to predict 3D canonical shape, deformation, viewpoint and texture from a single 2D image of a bird, given a bird video collection as well as automatically obtained silhouettes and optical flows as training data. Our method reconstructs temporally consistent 3D shape and deformation, which allows us to animate and re-render the bird from arbitrary viewpoints from a single image.

1 Introduction

Recently, with the adoption of machine learning, reconstructing 3D shapes from 2D images has advanced considerably. While this task traditionally requires establishing correspondences between multiple views [13], learning-based approaches have demonstrated the possibility of inferring 3D shapes from a single image, by learning priors for a specific object category [3, 9, 57, 12, 23, 10]. However, most of these methods rely on ground-truth 3D data [3, 9, 58, 57, 12, 23, 33, 43, 48, 10] or shape models [31, 19, 68, 49, 69] as supervision for training, and thus only work well on very specific categories, such as faces, human bodies and synthetic objects, where such data are available.

Recent unsupervised and weakly-supervised methods have shown promising reconstruction results on a wider variety of objects, by replacing the 3D ground-truth with weaker forms of supervision, such as 2D keypoints [20], 3D viewpoints [20, 39] and category-specific template shapes [25, 69, 11]. These additional sources of information provide strong supervisory signals for establishing correspondences between different instances, allowing the models to be trained on single-view image collections. Although these annotations are relatively cheaper compared to 3D ground-truth, it is still prohibitively difficult to collect such annotations for all object categories in the world at large scale.

In this paper, we aim to go one step further and leverage an even cheaper source of data to learn correspondences for reconstructing deformable 3D objects, which is “in-the-wild” monocular videos that are readily available online. Videos naturally provide rich correspondences across time as different views of the objects are observed. If the objects are static, existing methods [62, 29, 17] are able to learn 3D shapes based on similar principals as Structure-from-Motion (SfM) [5, 13]. However, many moving objects “in the wild”—such as animals—are not static, but rather highly deformable. Modeling these articulated shapes from monocular videos alone is very challenging due to the lack of multi-view consistency.

*Equal contribution.

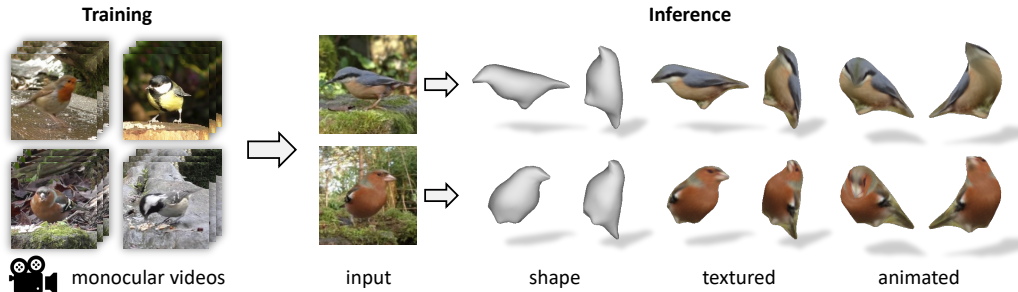


Figure 1: **DOVE - Deformable Objects from VidEos**. Given a collection of video clips of an object category as training data, we learn a model that is able to predict a textured, articulated 3D mesh of the object from a single input image.

In this work, we propose a method that automatically discovers and leverages correspondences in monocular videos for category-specific 3D reconstruction of deformable objects. Specifically, our model is trained on a collection of short video clips capturing objects of the same category, as illustrated in Fig. 1. To simplify the problem, here we assume videos with a static background, which are easy to obtain simply using a stationary camera (as is often done to capture wild animals), and rely on the object itself as the only source of motion, which is the exact opposite of [29]. Similar to previous methods [20, 11, 27], we also obtain 2D object masks using an off-the-shelf segmentation model, and assume bilateral symmetry in the shape and texture (but in the *canonical* pose rather than individual frames as in [20] due to asymmetric articulation), which is true for most animals. However, unlike these existing approaches, our method does not require explicit geometric supervision, such as keypoints, viewpoint or template shapes, and instead relies on the temporal information inherent in videos alone for learning 3D shapes.

To do this, we adopt a *photo-geometric auto-encoding* approach that disentangles shape, texture and pose of an object from each frame, with the objective of reconstructing the original image as well as the 2D object mask. Although on single frames this is an ill-posed problem, temporal consistency between consecutive frames in the videos provides powerful cues that make the problem tractable. First, the identity of the object remains the same in the video clip. By enforcing a constant base shape and texture, we can factor out the motion of the object with an articulation model and establish correspondences across different poses. As a result of this decomposition, we can also animate the objects with arbitrary poses, as shown in Fig. 1. Second, with videos, methods such as optical flow can be used to estimate 2D correspondences between frames automatically, which also provide geometric cues for recovering 3D shape and pose.

In summary, we present a method that learns to reconstruct deformable 3D object categories from “in-the-wild” monocular videos. By exploiting temporal consistency in videos, our method eliminates the need for explicit geometric supervision required by existing methods, such as keypoints, viewpoint or template shapes, which could potentially enable us to model a much wider range of objects where such annotations are difficult to obtain. Furthermore, our model produces temporally consistent reconstructions, whereas state-of-the-art methods produce inconsistent results as they are trained on independent, single images.

2 Related Work

Learning-based Reconstruction. A primary motivation for introducing machine learning in 3D reconstruction is to enable reconstruction from single views, which necessitates learning suitable shape priors. In particular, we focus the discussion on unsupervised and weakly-supervised methods that do not require explicit 3D ground-truth for training. Early unsupervised examples include monocular depth predictors trained from egocentric videos of rigid scenes, such as [8] and SfMLearner [67].

Other authors instead explored learning to reconstruct full 3D meshes of objects rather than depth maps [23, 20, 30, 22, 57, 42, 15, 11, 27, 28, 60]. Many of these works consider object categories and learn from still images only, generally using masks and additional sources of supervision or prior assumption: CMR [20] uses 2D keypoint annotations (in addition to masks) to initialize shape

Table 1: **Related Work.** Flow indicates optical flow. ¹coarse template shape and ²camera estimated from keypoints using SfM, ³outputs texture flow, ⁴shape bases initialized from CMR. *LASR and an online adaptation version of VMR have to be optimized on test sequences.

Method	Supervision						Output				
	Template	View	Keypoints	Mask	Flow	Video	3D	2.5D	Deform	View	Texture
VMR* [28]				✓		✓	✓		✓	✓	(✓) ³
LASR* [63]				✓	✓	✓	✓		✓	✓	✓
Unsup3D [59]								✓		✓	✓
CSM [25]	✓			✓						✓	✓
CMR [20]	(✓) ¹	(✓) ²	✓	✓			✓			✓	(✓) ³
U-CMR [11]	✓			✓			✓			✓	✓
UMR [27]				✓			✓			✓	(✓) ³
VMR [28]	(✓) ⁴	(✓) ²	✓	✓			✓		✓	✓	(✓) ³
Ours				✓	✓	✓	✓		✓	✓	✓

and viewpoint using SfM. U-CMR [11] extends CMR so that keypoint annotations are not required, but they require a template shape of the category beforehand. They also advocate for extensive view sampling (camera multiplex) to address the challenge of discovering the object viewpoint. UMR [27] replaces supervised keypoints with unsupervised part segmentations from SCOPS [18]. VMR [28] extends CMR and removes the symmetric shape assumption by constraining the base shape deformation with an As-Rigid-As-Possible (ARAP) [51] regularizer. Unsup3D [59] learns objects from still images, but only with limited viewpoint variation. CSM [25] and articulated CSM [26] learn to pose an externally-provided (articulated) 3D template of an object category to images while only using masks as supervision. We summarize the key differences in Table 1.

Adversarial learning can supplant the lack of multiple views of the same object. The idea is that the learned 3D model can be used to generate arbitrary views of an object, such that the discriminator network can provide supervisory signal to learn the geometry by telling whether the generated views are plausible or not. Examples include the works of [24, 2], PlatonicGAN [16], HoloGAN [37], BlockGAN [38], Shelf-supervised learning [64] and GRAF [50]. This type of approach does not require information about specific viewpoints, but does require to know the distribution of viewpoints in the training data (as the discriminator is sensitive to that). Overall, promising results can be achieved on synthetic data as well as a few real-life object categories, but general methods usually recover only very coarse 3D shapes or 3D feature volumes that are difficult to extract.

Reconstruction from Multiple Views and Videos. Most works using multiple views and videos focus on reconstructing individual instances of an object. Classic 3D reconstruction uses SfM pipelines from multiple views of a rigid scene, with pipelines such as KinectFusion [35] and DynamicFusion [36] integrating depth sensors for 3D reconstruction of dense static and deformable surfaces. NeRF [34] and its deformable extensions [44, 7, 55, 46, 40] such as D-NeRF [45] synthesize novel views from densely sampled multi-views of a static or mildly dynamic scene using a Neural Radiance Field, from which explicit 3D geometry can be further extracted. A more recent work, LASR [63], optimizes a single 3D deformable model on an individual video sequence.

Prior works on learning 3D categories from videos mostly focus on reconstruction of human bodies or faces [56, 1, 4, 21, 65, 6, 54]. However, they all require a shape prior, such as a parametric shape model [31]. [41] and [17] consider turn-table like videos to learn to reconstruct rigid object categories. VMR [28] introduces a test-time adaptation on individual videos that enforces temporal consistency of the shape and texture predictions obtained from a model pre-trained on object category images (apart from extending CMR as explained above). In contrast, our method learns a 3D shape model of a deformable object category from videos, which allows for single image reconstruction at inference.

3 Method

Our goal is to learn 3D shapes for a deformable object category from a collection of videos clips. Specifically, given a dataset of short video clips of the objects captured with stationary cameras, we would like to train a reconstruction model that takes as input a single image of an object and predicts the 3D shape, texture and articulated 3D pose of it. Fig. 2 gives an overview of the training pipeline.

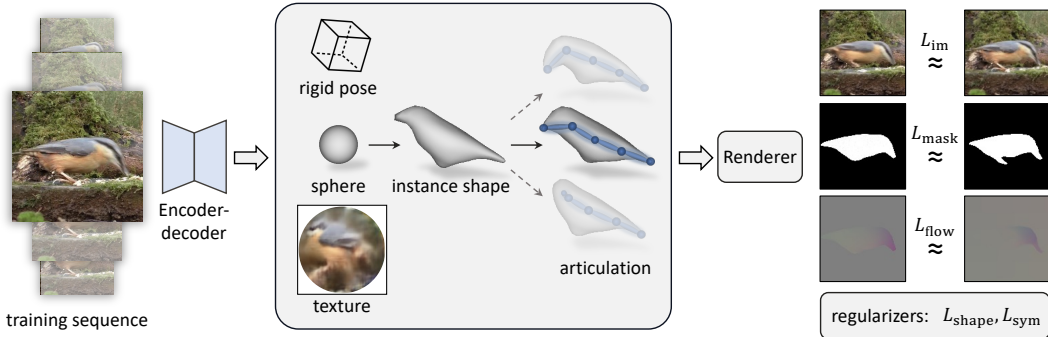


Figure 2: **Training Pipeline.** From a single frame of a video, we predict the 3D pose, shape and texture of the object. The shape is further disentangled into category shape, instance shape and deformation using bone skinning. Using a differentiable rendering step, we can train the model end-to-end by reconstructing the image and by enforcing temporal consistencies.

3.1 Photo-Geometric Auto-Encoding

Our reconstruction model takes in a single frame $I \in \mathbb{R}^{3 \times H \times W}$ from a video sequence and predicts the articulated 3D shape, texture and rigid pose of the object using three networks, denoted by f_S , f_T and f_P respectively. This information is then recombined to generate (render) an image of the object, which can be compared to the input video frames for supervision.

The shape is given by a triangulated mesh with fixed connectivity and variable vertex positions $V \in \mathbb{R}^{3 \times K}$. We distinguish instance-specific shape variations from frame-specific articulations by obtaining V in two steps, described next.

Instance-Specific Deformation. The first step is to reconstruct the shape V_{ins} of a specific video object instance in a canonical ‘rest pose’. This accounts for the fact that different object instances (e.g., different birds) have similar but different shapes. The shape is given by:

$$V_{\text{ins}} = V_{\text{cat}} + \Delta V_{\text{ins}}, \quad (1)$$

where V_{cat} is a learned category-specific template and ΔV_{ins} is the instance-specific shape variation.

We also assume that the object has a bilateral symmetry [59]. Vertices in this instance mesh are thus coupled in symmetric pairs by a permutation matrix $\Pi \in \{0, 1\}^{K \times K}$ (such that $\Pi^2 = I$). Furthermore, the bilateral symmetry plane of the object is mapped to the yz -plane in canonical space (an arbitrary choice). With this, a mesh V is symmetric if, and only if, $V\Pi = \text{diag}(-1, 1, 1)V$. In practice, we impose this constraint on both V_{cat} and ΔV_{ins} storing only half of the vertices and inferring the other half using this equation.

Articulation. In order to account for the effect of articulation, the object’s rest shape V_{ins} is further deformed by means of a *posing function* $V = g(V_{\text{ins}}, \xi)$ where ξ are the pose parameters. We model this function by means of a small number of virtual ‘bones’. Let \bar{V}_i be the homogeneous coordinates of a particular mesh vertex relative to a bone $b \in \{1, \dots, B\}$ to which it is rigidly attached, $\pi(b)$ the *parent* of bone b in the kinematic tree, and \mathbf{J}_b the location of the joint between the two bones expressed relative to the parent and let ξ_b be the parameters of the joint rotation. Then, we can express the vertex relative to the parent bone as $g_b(\xi)\bar{V}_i$ where:

$$g_b(\xi) = \begin{bmatrix} R_{\xi_b} & \mathbf{J}_b \\ 0 & 1 \end{bmatrix}.$$

Applying this construction recursively along the kinematic tree, we obtain the overall bone transformation $G_b = G_{\pi(b)} \circ g_b$, where the base case G_1 is the pose of the root joint w.r.t. the world. With this, the location of the vertex in the world is given by $V_i = G_b(\xi)\bar{V}_i$.

By inverting these relations, given the mesh V_{ins} at rest pose ξ_0 , we can express its vertices relative each bone as $\bar{V}_i = G_b(\xi_0)^{-1}[V_{\text{ins}}]_i$. As commonly done [31], we allow each vertex i to associate softly to one or more bones b via weights w_{bi} , obtaining the smoothed posing (or *skinning*) function:

$$V_i = \left(\sum_{b=1}^B w_{bi} G_b(\xi) G_b(\xi_0)^{-1} \right) [V_{\text{ins}}]_i. \quad (2)$$

Initialization. Unlike prior work such as [11], we do not assume that a category-specific, 3D template is available. Instead, we simply take a sphere as a base mesh V_{base} and optimize a set of vertex deformations $\Delta V_{\text{cat}} \in \mathbb{R}^{3 \times K}$ as trainable parameters. The category shape is then obtained by deforming the base shape as $V_{\text{cat}} = V_{\text{base}} + \Delta V_{\text{cat}}$. We also require to define the bone structure. Given the shape corresponding to the rest pose (after one epoch of training in a pose-free manner), we define a fixed number of bones inside the mesh that we set to lie on two line segments going from the two most extreme point of the mesh to the center. We then divide each line segment into equally-sized parts that define the origin and the length of each bone.

Shape and Pose Predictors. The final shape of the object V in each frame is thus expressed as:

$$V = g(V_{\text{ins}}, \xi) = g(V_{\text{base}} + \Delta V_{\text{cat}} + \Delta V_{\text{ins}}, \xi), \quad (3)$$

where V_{base} is fixed (a sphere), the template ΔV_{cat} is the same for all objects and treated as a vector of learnable parameters and the other quantities are predicted by networks from each input frame I . We predict the rigid pose of the object by means of a *rigid pose network* f_P as $(\xi_1, \mathbf{J}_1) = f_P(I|\theta)$. Recall that parameter ξ_1 corresponds to the root bone rotation, and \mathbf{J}_1 to its translation w.r.t. the world reference frame; together, they thus express the rigid component of the object pose. The instance-specific deformation and articulation parameters, ΔV_{ins} and ξ , are instead predicted by a *shape network*, also from the input frame: $(\Delta V_{\text{ins}}, \xi_{2:B}) = f_S(I|\theta)$.

Appearance Model and Differentiable Rendering. We represent the texture of the object using a texture map $T \in \mathbb{R}^{3 \times H_T \times W_T}$. The vertices of the base mesh V_{base} are assigned to fixed texture uv-coordinates and the texture inherits the symmetry of the base mesh. Formally, this means that the mesh vertices $V_{\text{base}} \in \mathbb{R}^{3 \times K}$ are mapped to uv-coordinates $U \in \mathbb{R}^{2 \times K}$ such that $U\Pi = U$.

The texture is also predicted from the video frame I by a *texture network* f_T as $T = f_T(I|\theta)$. Given the posed mesh V and the texture T , we can then *render* an image $\hat{I} = \mathcal{R}(V, T)$ of the object using standard perspective-correct texture mapping with barycentric coordinates. We also render the 2D mask of the object as $\hat{M} = \mathcal{R}(V)$. Specifically, we use the PyTorch3D differentiable mesh renderer [47]. We overlay the rendered mesh to the background of the object. Since the camera is fixed, the latter can easily be extracted from frames where the objects is not detected, which are then averaged (an alternative to restricting the photometric loss described below to the masked pixels).

3.2 Learning from Videos

Our goal is to learn the reconstruction model from a collection of video sequences $\mathcal{S} = \{S_i\}_{i=1}^{|\mathcal{S}|}$, where each sequence S_i consists of frames $S_i = (I_{it}, M_{it})_{t=1}^{|S_i|}$ cropped around object instances. Here, i denotes the sequence index and t the frame index (time). These sequences are obtained by pre-processing the videos using an off-the-shelf instance segmentation technique (Mask R-CNN [14]).

Temporal Consistency. One important property of the frames in a video track is that they show the *same* object instances and thus share the same instance-specific shape $V_{\text{ins},i}$ and texture T_i . Recall, however, that different shapes $V_{\text{ins},i}$ and textures T_i are predicted from individual frames I_{it} by networks f_S and f_T . We encourage these predictions to be consistent (constant) for a sequence by randomly replacing them with their sequence-wise averages $\Delta V_{\text{ins},i} = \frac{1}{|S_i|} \sum_{t=1}^{|S_i|} \Delta V_{\text{ins},it}$ and $T_i = \frac{1}{|S_i|} \sum_{t=1}^{|S_i|} T_{it}$ for rendering. The idea is that inconsistent textures will lead to blurry averages and thus higher reconstruction error. This encourages temporally consistent textures.

Rendering Losses. Given a training image I_{it} and a corresponding mask M_{it} , we first consider the image reconstruction loss:

$$L_{\text{im},it} = \|\hat{I}_{it} - I_{it}\|_1, \quad \text{where } \hat{I}_{it} = \mathcal{R}(V_{it}, T_i) \text{ and } V_{it} = g(V_{\text{base}} + \Delta V_{\text{cat}} + \Delta V_{\text{ins},i}, \xi_{it}). \quad (4)$$

As explained above, the instance shape $\Delta V_{\text{ins},i}$ and texture T_i are sequence averages, independent of the time index t . We also define a similar loss for the rendered mask:

$$L_{\text{mask},it} = \lambda_m \|\hat{M}_{it} - M_{it}\|_2^2 + \lambda_{\text{dt}} \|\text{dt}(\hat{M}_{it}) \odot \hat{M}_{it}\|_1, \quad \text{where } \hat{M}_{it} = \mathcal{R}(V_{it}), \quad (5)$$

$\text{dt}(\cdot)$ is the distance transform of the mask, \odot denotes Hadamard product, and λ_m and λ_{dt} are the balancing weights. Additionally, we also use a perceptual loss [66] between image and reconstruction that helps to recover sharper images and textures.

Optical Flow. Another advantage of videos is that 2D correspondences between consecutive video frames can be estimated accurately and robustly using optical flows and can be used as a supervisory signal. To this end, let $F_{it} \in \mathbb{R}^{H \times W \times 2}$ be the optical flow image between frames t and $t + 1$ (we use the off-the-shelf RAFT model [52]). We define an *optical flow loss*:

$$L_{\text{flow},it} = \|\hat{F}_{it} - F_{it}\|_2^2, \quad (6)$$

where \hat{F}_{it} is the flow image derived from the predicted geometry. Computing the flow for the mesh vertices is easy, but this needs to be interpolated for all image pixels. We do this by ‘recycling’ the differentiable renderer. First, we compute the 2D displacement for the shape vertices projected to image plane $\delta_{it} = \pi(V_{i,t+1} - V_{it}) \in \mathbb{R}^{2 \times K}$. We can then use the renderer to render an optical flow image by simply treating these 2D displacement vectors as vertex colors: $\hat{F}_{it} = \mathcal{R}(V_{it}, \delta_{it})$.

3.3 Additional Regularization and Overall Objective

Posing Symmetry. We have assumed that objects have a bilateral symmetry, which is easily enforced in canonical rest pose. However, we can also enforce that the *space of poses* is symmetric too [53].² To this end, let ηI denote an image flipped horizontally. Furthermore, overload the same operator so that its action on a pose $\eta\xi$ is to flip the pose w.r.t. the horizontal axis (formally $G_b(\eta\xi) = \text{diag}(-1, 1, 1)G_{\Pi_b}(\xi)\text{diag}(-1, 1, 1)$ where Π_b is the symmetric counterpart of bone b). Then, we minimize the loss:

$$L_{\text{sym},it} = \|f_P(\eta I_{it}) - \eta(f_P(I_{it}))\|_2^2. \quad (7)$$

In our experiments, since the deformation of the birds is rather simple, we only impose this constraint on the rigid pose (*i.e.* $b = 1$).

Geometric Smoothing. We also use smoothing losses for the 3D geometry that are typical in the computer graphics literature. To prevent the instance-specific shapes from unreasonable deviations from the category prior, we add an As-Rigid-As-Possible (ARAP) regularizer [51] between the prior shape and the instance shapes:

$$L_{\text{ins},i} = \sum_{k=1}^K \min_{R \in SO(3)} \sum_{j \in \mathcal{N}_k} w_{jk} \|([V_{\text{ins},i}]_j - [V_{\text{ins},i}]_k) - R([V_{\text{cat},i}]_j - [V_{\text{cat},i}]_k)\|^2, \quad (8)$$

where \mathcal{N}_k is the fan of vertices around vertex k . ARAP thus encourages triangle fans to deform rigidly. We also add a Laplacian smoothing loss and a normal consistency loss on the instance shapes:

$$L_{\text{Lap},i} = \sum_{k=1}^K \left\| [V_{\text{ins},i}]_k - \frac{1}{|\mathcal{N}_k|} \sum_{j \in \mathcal{N}_k} [V_{\text{ins},i}]_j \right\|^2, \quad L_{\text{nrn},i} = \sum_{f \in \mathcal{F}} \sum_{f' \in \mathcal{N}_f} \left(1 - \frac{\mathbf{n}_{if} \cdot \mathbf{n}_{if'}}{\|\mathbf{n}_{if}\| \|\mathbf{n}_{if'}\|} \right), \quad (9)$$

where \mathbf{n}_{if} is the normal of face f in $V_{\text{ins},i}$ and \mathcal{N}_f are the faces adjacent to f in the mesh. We sum the three geometric losses in the shape regularizer $L_{\text{shape},i} = \lambda_{\text{ins}}L_{\text{ins},i} + \lambda_{\text{Lap}}L_{\text{Lap},i} + \lambda_{\text{nrn}}L_{\text{nrn},i}$.

Overall Learning Objective. The final loss is the weighted sum of individual terms:

$$L = \frac{1}{|\mathcal{S}|} \sum_{i=1}^{|\mathcal{S}|} \left(L_{\text{shape},i} + \frac{1}{|\mathcal{S}_i|} \sum_{t=1}^{|\mathcal{S}_i|} (L_{\text{im},it} + L_{\text{mask},it} + \lambda_{\text{flow}}L_{\text{flow},it} + \lambda_{\text{sym}}L_{\text{sym},it}) \right). \quad (10)$$

4 Experiments

4.1 Dataset and Implementation Details

Dataset. We extract a large number of short video clips of birds from YouTube, searching for ‘‘bird videos for cats’’.³ Mask R-CNN [14] is then used to detect and segment bird instances and the videos are automatically split into short clips, each containing a single bird. The images and the masks are cropped around the birds and resized to 128×128 for training. We also run the

²Note the individual poses are not symmetric, but we can find a symmetric counterpart for any given pose.

³All clips are extracted from an 8h video by Paul Dinning available at <https://youtu.be/xbs7FT7dXYc>.

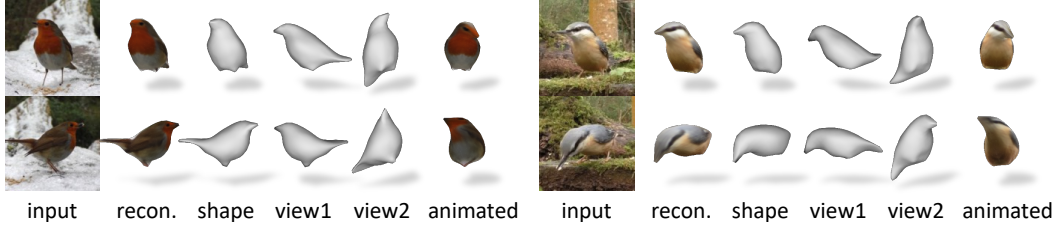


Figure 3: **Qualitative Examples.** We show multiple views of the reconstructed mesh together with a textured view and animated version of the bird that we obtained by rotating the learned bones. We find that the model is able to recover the shape well even when seen from novel viewpoints. The animation is able to generate believable poses.

Table 2: **Mask Reprojection IoU.** We measure the shape reconstruction quality and temporal consistency via the mean intersection over union (mIoU) of reprojected masks. We take the predicted shape at frame t and reproject it with the camera pose of frame $t + \Delta t$. The higher the better.

frame offset	$\Delta t = 0$	$\Delta t = 5$	$\Delta t = 10$
CMR [20] (finetuned)	0.786 \pm 0.131	0.759 \pm 0.135	0.749 \pm 0.135
U-CMR [11] (finetuned)	0.799 \pm 0.059	0.786 \pm 0.067	0.782 \pm 0.069
VMR [28] (finetuned)	0.821 \pm 0.068	0.793 \pm 0.080	0.780 \pm 0.083
UMR [27] (finetuned)	0.852 \pm 0.042	0.818 \pm 0.067	0.805 \pm 0.070
UMR [27] (from scratch)	0.839 \pm 0.042	0.803 \pm 0.067	0.789 \pm 0.071
Ours (articulation fixed)	0.871 \pm 0.065	0.835 \pm 0.083	0.820 \pm 0.086
Ours (articulation transferred)	0.871 \pm 0.065	0.859 \pm 0.068	0.853 \pm 0.068

off-the-shelf RAFT model [52] on the full frames to estimate optical flow between consecutive frames, and account for the cropping and resizing to obtain the correct optical flow for the crops. With this procedure, we collected 2,269 sequences with paired image, mask and flow, each containing 16 to a few hundred frames, totaling 170,755 frames. We randomly split them into 2,097 training and 172 testing sequences.

Implementation Details. Our reconstruction model is implemented using three neural networks (f_S, f_P, f_T) as well as a set of trainable parameters for the categorical prior shape ΔV_{cat} . The shape network f_S and the rigid pose network f_P are simple encoders with downsampling convolutional layers that take in an image and predict vertex deformations ΔV_{ins} , skinning parameters $\xi_{2:B}$, and rigid pose ξ_1 and \mathbf{J}_1 as flattened vectors. The texture network f_T is an encoder-decoder that predicts the texture map T from an image. We use Adam optimizers with a learning rate of 0.0001 for all networks, and a learning rate 0.01 for the category shape parameters ΔV_{cat} . All images resized to 128×128 . We use a symmetric ico-sphere with 642 vertices and 1,280 triangles as the initial mesh. For each training iteration, we randomly sample 8 consecutive frames from 8 sequences. The models are trained from scratch for 10 epochs with which takes roughly 3 days on one NVIDIA RTX-6000 GPU. During the first epoch we disable the instance shape and frame-specific deformation to learn a reasonable prior shape first. All details are included in the supplementary material.

4.2 Qualitative Results

Figure 3 shows single frame reconstruction results obtained from our model. Note that videos are no longer required during inference. Despite not requiring any explicit 3D, viewpoint or keypoint supervision, our model learns to reconstruct accurate 3D shapes from only monocular training videos. We can animate the reconstructed 3D bird with our skinning model by adjusting the bone rotations.

4.3 Comparisons with State-of-the-Art Methods

We compare our model with a number of state-of-the-art learning-based reconstruction methods, including CMR [20], U-CMR [11], UMR [27] and VMR [28]. CMR requires 2D keypoint annotations for initializing the 3D shape and viewpoints and also for the training loss. U-CMR removes keypoint supervision but requires a 3D template shape to begin with, and UMR replaces that with self-supervised part segmentation maps using SCOPS [18] which requires supervised ImageNet

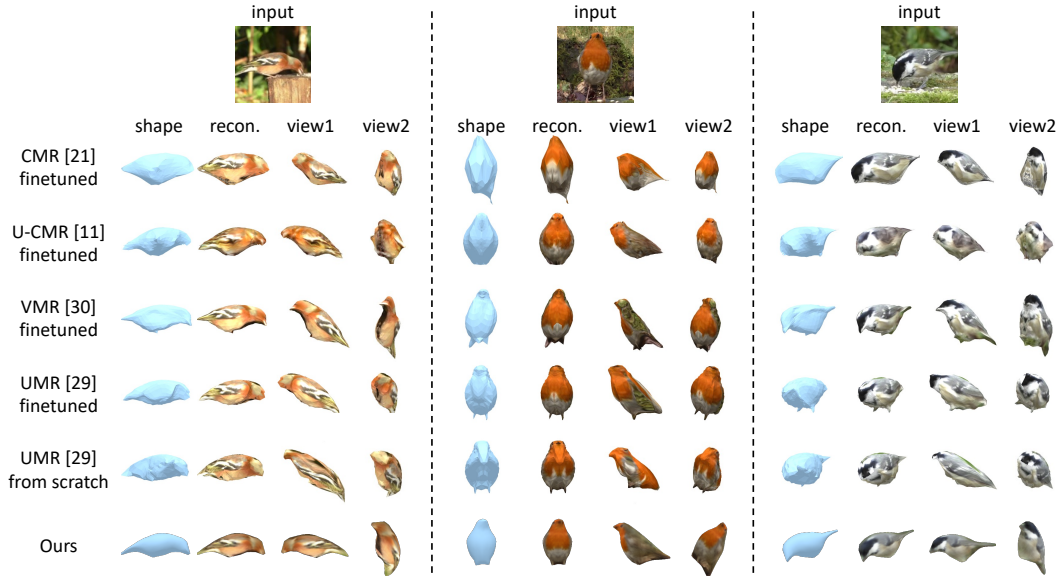


Figure 4: **Visual Comparison.** We compare our reconstructions to state-of-the-art methods by finetuning their models on our dataset. Our method consistently reconstructs reasonable 3D shapes, whereas others produce poor shapes for certain input poses.

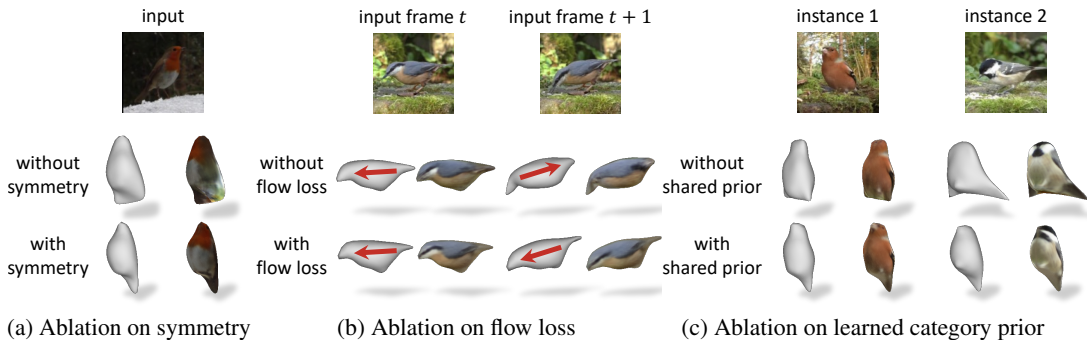


Figure 5: **Ablation.** We train our model without some of the key components: a) symmetry assumption, b) optical flow and c) a learned base shape across sequences. All parts fulfill a specific role in the reconstruction pipeline that regularize the learned 3D shape and pose.

pretraining. VMR [28] allows for deformations but it requires the same level of supervision as CMR. VMR also introduces an optional test-time optimization procedure that adapts their pre-trained model on individual test videos to improve temporal consistency. The authors also present a self-supervised variant of VMR that uses only segmentation masks for supervision but produces worse results, and we were not able to reproduce it. For evaluation, we consider the first and the second (in Section 6.4) versions of VMR. We finetuned the trained models for all four methods on our dataset. We also trained UMR from scratch with SCOPS predictions obtained from a pre-trained SCOPS model.

Quantitative Comparisons. We evaluate the methods on our video test set. Since we do not have ground-truth 3D shape for direct evaluation, we measure reconstruction quality via a mask reprojection accuracy from one frame to another, using the object masks predicted by Mask R-CNN [14] as the pseudo ground-truth. For each test sequence, we predict the shape at frame t and render the object mask from the pose at frame $t + \Delta t$ with an offset Δt of 0, 5 and 10 frames. We then compute the mean Intersection over Union (mIoU) between the rendered masks and the ground-truth masks over all frames. This metric not only measures the accuracy of the predicted shape, but also its consistency over time. Table 2 summarizes the results, which suggests that our model achieves both better shape reconstruction and temporal consistency. We also compute the metrics on our model with frame-specific deformations predicted at frame $t + \Delta t$ applied to the shape predicted at frame t . This further improves the mask reprojection IoU, which confirms that our model learns correct

frame-specific deformations. Other methods overfit their projected shape to a single frame, resulting in a larger decrease in reprojection accuracy with increasing frame offset Δt .

Qualitative Comparisons. Fig. 4 shows a qualitative comparison of different methods. Among previous methods, CMR produces the most robust reconstructions as it relies on keypoint supervision, but still performs poorly for challenging poses, such as frontal views. Our method reconstructs accurate shape and pose, despite not using keypoint or template supervision. Moreover, the reconstructions obtained by our method are more consistent temporally compared to other methods. We refer the reader to the animations on our project website for more results. Note that our model is trained on 128×128 images, whereas other methods train on 256×256 images and, except U-CMR, sample the texture from the input image, hence the difference in the texture quality.

4.4 Ablation and Analysis

Symmetry. To understand the effect of symmetry, we ablate the model by training it without the symmetry constraint on the rest-pose shape and on the texture. Figure 5a shows an example of the comparison with our full model. The model without symmetry produces unrealistic shapes indicating that symmetry is a useful prior, even when learning deformable shapes.

Optical Flow. We analyze the effect of the optical flow loss by comparing the results with and without the flow loss. An example is shown in Fig. 5b. Without the flow loss, the model produces inconsistent reconstructions in ambiguous poses and tends to confuse head and tail of the birds. The optical flow helps resolve such ambiguities and improves temporal consistency.

Prior Shape. We train another model without the learned category prior shape, predicting individual shapes for each bird. The resulting reconstructions are inconsistent across different instances, shown in Fig. 5c. This suggests that the full model is able to leverage shape prior of the whole category to predict the instance shapes, which is a major benefit of learning in a reconstruction pipeline.

4.5 Limitations

In this section we identify several weaknesses of our model. Due to the nature of the videos—seeds in front of the camera—the vast majority of clips show the birds from front and side positions. This results in degraded performance when the bird is facing away from the camera and the pose predictions rarely exceed ± 90 deg.

In terms of supervision, we still require segmentation masks obtained from the off-the-shelf model and their quality affects the fidelity of our reconstructions. Thus, similar to comparable methods, our reconstructions do not capture fine details such as legs and the beak. The texture prediction sometimes results in low quality reconstructions especially when the input image is affected by motion blur.

In view of extending this method to other animal categories such as dogs or horses, birds have a rather simple geometry and deformation structure, which might not generalize well.

5 Conclusions

We have presented a method to learn articulated 3D representations of deformable objects from monocular videos without explicit geometric supervision, such as keypoints, viewpoint or template shapes. The resulting 3D meshes are temporally consistent and can be animated. The method can be trained from YouTube videos and only needs off-the-shelf object detection and optical flow models for data preprocessing. In the future, we hope to extend the presented approach to more categories, such as horses and cats, as training data is readily available for those as well.

Broader Impact Our work focuses on 3D reconstruction of deformable objects from monocular videos. We expect this work to be most useful for object categories that do not have sophisticated 3D ground-truth annotations and 3D shape models. This is mainly the case for animals, as shown for birds here, and thus the work can potentially be of use in behavioral research of animals in the wild. Our dataset does not contain any humans, only birds in nature background and thus does not violate personal privacy of individuals. The dataset has some bias as according to the author, the video clips were recorded in the UK and thus only depict bird species that appear there. Overall, we expect this work to impact mostly the research community with very little impact on society in the short term.

Acknowledgments

We thank Xueting Li for sharing the code for VMR with us. Shangzhe Wu is supported by Facebook Research. Tomas Jakab is supported by Clarendon Scholarship. Christian Rupprecht is supported by Innovate UK (project 71653) on behalf of UK Research and Innovation (UKRI) and by the European Research Council (ERC) IDIU-638009. Andrea Vedaldi is supported by European Research Council (ERC) IDIU-638009.

References

- [1] Anurag Arnab, Carl Doersch, and Andrew Zisserman. Exploiting temporal context for 3d human pose estimation in the wild. In *CVPR*, pages 3395–3404, 2019.
- [2] Ching-Hang Chen, Amrith Tyagi, Amit Agrawal, Dylan Drover, Rohith MV, Stefan Stojanov, and James M. Rehg. Unsupervised 3d pose estimation with geometric self-supervision. In *CVPR*, 2019.
- [3] Christopher B Choy, Danfei Xu, JunYoung Gwak, Kevin Chen, and Silvio Savarese. 3d-r2n2: A unified approach for single and multi-view 3d object reconstruction. In *ECCV*, 2016.
- [4] Carl Doersch and Andrew Zisserman. Sim2real transfer learning for 3d human pose estimation: motion to the rescue. *NeurIPS*, 32:12949–12961, 2019.
- [5] Olivier Faugeras and Quang-Tuan Luong. *The Geometry of Multiple Images*. MIT Press, 2001.
- [6] Yao Feng, Fan Wu, Xiaohu Shao, Yanfeng Wang, and Xi Zhou. Joint 3d face reconstruction and dense alignment with position map regression network. In *ECCV*, pages 534–551, 2018.
- [7] Guy Gafni, Justus Thies, Michael Zollhöfer, and Matthias Nießner. Dynamic neural radiance fields for monocular 4d facial avatar reconstruction. In *CVPR*, 2021.
- [8] Ravi Garg, B. G. Vijay Kumar, Gustavo Carneiro, and Ian D. Reid. Unsupervised CNN for single view depth estimation: Geometry to the rescue. In *ECCV*, 2016.
- [9] Rohit Girdhar, David Fouhey, Mikel Rodriguez, and Abhinav Gupta. Learning a predictable and generative vector representation for objects. In *ECCV*, 2016.
- [10] Georgia Gkioxari, Jitendra Malik, and Justin Johnson. Mesh r-cnn. In *ICCV*, 2019.
- [11] Shubham Goel, Angjoo Kanazawa, and Jitendra Malik. Shape and viewpoint without keypoints. In *ECCV*, 2020.
- [12] Thibault Groueix, Matthew Fisher, Vladimir G. Kim, Bryan Russell, and Mathieu Aubry. AtlasNet: A Papier-Mâché Approach to Learning 3D Surface Generation. In *CVPR*, 2018.
- [13] Richard Hartley and Andrew Zisserman. *Multiple View Geometry in Computer Vision*. Cambridge University Press, ISBN: 0521540518, second edition, 2004.
- [14] Kaiming He, Georgia Gkioxari, Piotr Dollár, and Ross B. Girshick. Mask R-CNN. In *ICCV*, 2017.
- [15] Paul Henderson and Vittorio Ferrari. Learning single-image 3d reconstruction by generative modelling of shape, pose and shading. *IJCV*, pages 1–20, 2019.
- [16] Philipp Henzler, Niloy J. Mitra, and Tobias Ritschel. Escaping plato’s cave using adversarial training: 3D shape from unstructured 2D image collections. In *ICCV*, 2019.
- [17] Philipp Henzler, Jeremy Reizenstein, Patrick Labatut, Roman Shapovalov, Tobias Ritschel, Andrea Vedaldi, and David Novotny. Unsupervised learning of 3d object categories from videos in the wild. In *CVPR*, 2021.
- [18] Wei-Chih Hung, Varun Jampani, Sifei Liu, Pavlo Molchanov, Ming-Hsuan Yang, and Jan Kautz. SCOPS: self-supervised co-part segmentation. In *CVPR*, 2019.
- [19] Angjoo Kanazawa, Michael J. Black, David W. Jacobs, and Jitendra Malik. End-to-end recovery of human shape and pose. In *CVPR*, 2018.
- [20] Angjoo Kanazawa, Shubham Tulsiani, Alexei A. Efros, and Jitendra Malik. Learning category-specific mesh reconstruction from image collections. In *ECCV*, 2018.
- [21] Angjoo Kanazawa, Jason Y Zhang, Panna Felsen, and Jitendra Malik. Learning 3d human dynamics from video. In *CVPR*, pages 5614–5623, 2019.
- [22] Hiroharu Kato and Tatsuya Harada. Learning view priors for single-view 3d reconstruction. In *CVPR*, pages 9778–9787, 2019.
- [23] Hiroharu Kato, Yoshitaka Ushiku, and Tatsuya Harada. Neural 3d mesh renderer. In *CVPR*, 2018.

- [24] Yasunori Kudo, Keisuke Ogaki, Yusuke Matsui, and Yuri Odagiri. Unsupervised adversarial learning of 3D human pose from 2D joint locations. *arXiv preprint arXiv:1803.08244*, 2018.
- [25] Nilesh Kulkarni, Abhinav Gupta, and Shubham Tulsiani. Canonical surface mapping via geometric cycle consistency. In *ICCV*, 2019.
- [26] Nilesh Kulkarni, Abhinav Gupta, David F. Fouhey, and Shubham Tulsiani. Articulation-aware canonical surface mapping. In *CVPR*, pages 449–458, 2020.
- [27] Xueting Li, Sifei Liu, Kihwan Kim, Shalini De Mello, Varun Jampani, Ming-Hsuan Yang, and Jan Kautz. Self-supervised single-view 3D reconstruction via semantic consistency. In *ECCV*, 2020.
- [28] Xueting Li, Sifei Liu, Shalini De Mello, Kihwan Kim, Xiaolong Wang, Ming-Hsuan Yang, and Jan Kautz. Online adaptation for consistent mesh reconstruction in the wild. In *NeurIPS*, 2020.
- [29] Zhengqi Li, Tali Dekel, Forrester Cole, Richard Tucker, Noah Snavely, Ce Liu, and William T. Freeman. Learning the depths of moving people by watching frozen people. In *CVPR*, 2019.
- [30] Shichen Liu, Tianye Li, Weikai Chen, and Hao Li. Soft rasterizer: A differentiable renderer for image-based 3d reasoning. In *ICCV*, 2019.
- [31] Matthew Loper, Naureen Mahmood, Javier Romero, Gerard Pons-Moll, and Michael J. Black. SMPL: a skinned multi-person linear model. *ACM TOG*, 2015.
- [32] Andrew L. Maas, Awni Y. Hannun, and Andrew Y. Ng. Rectifier nonlinearities improve neural network acoustic models. In *ICML*, 2013.
- [33] Lars Mescheder, Michael Oechsle, Michael Niemeyer, Sebastian Nowozin, and Andreas Geiger. Occupancy networks: Learning 3d reconstruction in function space. In *CVPR*, 2019.
- [34] Ben Mildenhall, Pratul P. Srinivasan, Matthew Tancik, Jonathan T. Barron, Ravi Ramamoorthi, and Ren Ng. NeRF: Representing scenes as neural radiance fields for view synthesis. In *ECCV*, 2020.
- [35] Richard A. Newcombe, Shahram Izadi, Otmar Hilliges, David Molyneaux, David Kim, Andrew J. Davison, Pushmeet Kohli, Jamie Shotton, Steve Hodges, and Andrew W. Fitzgibbon. KinectFusion: Real-time dense surface mapping and tracking. In *Proc. ISMAR*, 2011.
- [36] Richard A. Newcombe, Dieter Fox, and Steven M. Seitz. DynamicFusion: Reconstruction and tracking of non-rigid scenes in real-time. In *CVPR*, 2015.
- [37] Thu Nguyen-Phuoc, Chuan Li, Lucas Theis, Christian Richardt, and Yong-Liang Yang. Hologan: Unsupervised learning of 3d representations from natural images. In *ICCV*, 2019.
- [38] Thu Nguyen-Phuoc, Christian Richardt, Long Mai, Yong-Liang Yang, and Niloy J. Mitra. Blockgan: Learning 3d object-aware scene representations from unlabelled images. In *NeurIPS*, 2020.
- [39] Michael Niemeyer, Lars Mescheder, Michael Oechsle, and Andreas Geiger. Differentiable volumetric rendering: Learning implicit 3d representations without 3d supervision. In *CVPR*, 2020.
- [40] Atsuhiko Noguchi, Xiao Sun, Stephen Lin, and Tatsuya Harada. Neural articulated radiance field. *arXiv preprint arXiv:2104.03110*, 2021.
- [41] David Novotný, Diane Larlus, and Andrea Vedaldi. Learning 3D object categories by looking around them. In *ICCV*, 2017.
- [42] Junyi Pan, Xiaoguang Han, Weikai Chen, Jiapeng Tang, and Kui Jia. Deep mesh reconstruction from single rgb images via topology modification networks. In *ICCV*, pages 9964–9973, 2019.
- [43] Jeong Joon Park, Peter Florence, Julian Straub, Richard Newcombe, and Steven Lovegrove. DeepSDF: Learning continuous signed distance functions for shape representation. In *CVPR*, June 2019.
- [44] Keunhong Park, Utkarsh Sinha, Jonathan T Barron, Sofien Bouaziz, Dan B Goldman, Steven M Seitz, and Ricardo-Martín Brualdi. Deformable neural radiance fields. *arXiv preprint arXiv:2011.12948*, 2020.
- [45] Albert Pumarola, Enric Corona, Gerard Pons-Moll, and Francesc Moreno-Noguer. D-NeRF: Neural Radiance Fields for Dynamic Scenes. In *CVPR*, 2020.
- [46] Amit Raj, Michael Zollhoefer, Tomas Simon, Jason Saragih, Shunsuke Saito, James Hays, and Stephen Lombardi. Pva: Pixel-aligned volumetric avatars. *arXiv preprint arXiv:2101.02697*, 2020.
- [47] Nikhila Ravi, Jeremy Reizenstein, David Novotny, Taylor Gordon, Wan-Yen Lo, Justin Johnson, and Georgia Gkioxari. Accelerating 3d deep learning with pytorch3d. *arXiv preprint arXiv:2007.08501*, 2020.
- [48] Shunsuke Saito, Zeng Huang, Ryota Natsume, Shigeo Morishima, Angjoo Kanazawa, and Hao Li. Pifu: Pixel-aligned implicit function for high-resolution clothed human digitization. In *ICCV*, 2019.

- [49] Soubhik Sanyal, Timo Bolkart, Haiwen Feng, and Michael Black. Learning to regress 3D face shape and expression from an image without 3D supervision. In *CVPR*, 2019.
- [50] Katja Schwarz, Yiyi Liao, Michael Niemeyer, and Andreas Geiger. Graf: Generative radiance fields for 3d-aware image synthesis. In *NeurIPS*, 2020.
- [51] Olga Sorkine and Marc Alexa. As-rigid-as-possible surface modeling. In *Symposium on Geometry processing*, volume 4, pages 109–116, 2007.
- [52] Zachary Teed and Jia Deng. RAFT: recurrent all-pairs field transforms for optical flow. In *ECCV*, 2020.
- [53] James Thewlis, Hakan Bilen, and Andrea Vedaldi. Modelling and unsupervised learning of symmetric deformable object categories. In *NeurIPS*, 2018.
- [54] Luan Tran and Xiaoming Liu. On learning 3d face morphable model from in-the-wild images. *IEEE TPAMI*, 43(1):157–171, 2019.
- [55] Edgar Tretschk, Ayush Tewari, Vladislav Golyanik, Michael Zollhöfer, Christoph Lassner, and Christian Theobalt. Non-rigid neural radiance fields: Reconstruction and novel view synthesis of a dynamic scene from monocular video. *arXiv preprint arXiv:2012.12247*, 2020.
- [56] Hsiao-Yu Tung, Hsiao-Wei Tung, Ersin Yumer, and Katerina Fragkiadaki. Self-supervised learning of motion capture. In *NIPS*, 2017.
- [57] Nanyang Wang, Yinda Zhang, Zhuwen Li, Yanwei Fu, Wei Liu, and Yu-Gang Jiang. Pixel2mesh: Generating 3d mesh models from single rgb images. In *ECCV*, 2018.
- [58] Jiajun Wu, Chengkai Zhang, Tianfan Xue, William T Freeman, and Joshua B Tenenbaum. Learning a probabilistic latent space of object shapes via 3d generative-adversarial modeling. In *NeurIPS*, pages 82–90, 2016.
- [59] Shangzhe Wu, Christian Rupprecht, and Andrea Vedaldi. Unsupervised learning of probably symmetric deformable 3D objects from images in the wild. In *CVPR*, 2020.
- [60] Shangzhe Wu, Ameesh Makadia, Jiajun Wu, Noah Snavely, Richard Tucker, and Angjoo Kanazawa. De-rendering the world’s revolutionary artefacts. In *CVPR*, 2021.
- [61] Yuxin Wu and Kaiming He. Group normalization. In *ECCV*, 2018.
- [62] Christopher Xie, Keunhong Park, Ricardo Martin-Brualla, and Matthew Brown. Fig-nerf: Figure-ground neural radiance fields for 3d object category modelling. *arXiv preprint arXiv:2104.08418*, 2021.
- [63] Gengshan Yang, Deqing Sun, Varun Jampani, Daniel Vlasic, Forrester Cole, Huiwen Chang, Deva Ramanan, William T. Freeman, and Ce Liu. LASR: Learning articulated shape reconstruction from a monocular video. In *CVPR*, 2021.
- [64] Yufei Ye, Shubham Tulsiani, and Abhinav Gupta. Shelf-supervised mesh prediction in the wild. In *CVPR*, 2021.
- [65] Jason Y Zhang, Panna Felsen, Angjoo Kanazawa, and Jitendra Malik. Predicting 3d human dynamics from video. In *ICCV*, pages 7114–7123, 2019.
- [66] Richard Zhang, Phillip Isola, Alexei A Efros, Eli Shechtman, and Oliver Wang. The unreasonable effectiveness of deep features as a perceptual metric. In *CVPR*, 2018.
- [67] Tinghui Zhou, Matthew Brown, Noah Snavely, and David G. Lowe. Unsupervised learning of depth and ego-motion from video. In *CVPR*, 2017.
- [68] Silvia Zuffi, Angjoo Kanazawa, David Jacobs, and Michael J. Black. 3D menagerie: Modeling the 3D shape and pose of animals. In *CVPR*, 2017.
- [69] Silvia Zuffi, Angjoo Kanazawa, Tanja Berger-Wolf, and Michael J. Black. Three-d safari: Learning to estimate zebra pose, shape, and texture from images "in the wild". In *ICCV*, 2019.

6 Supplementary Materials

6.1 Model Details

Shape and Texture. For the base shape, we use an ico-sphere with 642 vertices and 1,280 faces. Since the texture is symmetric, we compute the texture coordinates of both half spheres by unwrapping a half sphere onto the plane as illustrated in Fig. 6. Mathematically, this is computed as:

$$u = \frac{2 \arccos |x|}{\pi} \frac{z}{\sqrt{z^2 + y^2}}, \quad v = \frac{2 \arccos |x|}{\pi} \frac{y}{\sqrt{z^2 + y^2}}. \quad (11)$$

Rigid Pose. We represent the rigid rotation of the object using Euler angles about the xy -axes, with azimuth ranging from -180° to 180° and elevation ranging from -90° to 90° , and disable the rotation about z -axis as the birds do not roll significantly on the ground. As a result, the body roll movement is factored into the articulation model, as illustrated by the 4-th principal component in the learned articulation model in Fig. 8. The translations in xyz -axes are capped at a range roughly corresponding to half of the image size.

Skinning Model. As described in the main paper, we estimate the bone structure using the two most extreme points of the mesh at its rest pose. The one with positive z coordinate is selected as the head end and the other one the tail end, ensuring consistent orientation of the bone structure. The rotation of individual bones is represented using Euler angles about the xyz -axes in its local coordinate frame, where the center of rotation is specified by the joint location.

Recall Eq. (2) of the main paper where we use skinning weights w_{bi} that associate each mesh vertex with the bones. We softly assign each mesh vertex with the bones based on its distances to the bones. The weights are defined as the inverse of the distance between a vertex $[V_{\text{ins}}]_i$ and a bone b at their rest pose. We normalize this distance for each vertex over all the bones with softmax function:

$$w_{bi} = \frac{e^{d_{bi}}}{\sum_{k=1}^B e^{d_{ki}}}, \quad d_{bi} = 1 / \left(\min_{r \in [0,1]} \|[V_{\text{ins}}]_i - r\mathbf{s}_{b1} - (1-r)\mathbf{s}_{b2}\|_2^2 + \epsilon \right), \quad (12)$$

where $(\mathbf{s}_{b1}, \mathbf{s}_{b2})$ is the line segment defining the bone b at its rest pose and ϵ is a small number to avoid division by zero.

6.2 Network Architectures

All the network architectures are described in in Table 3 and Section 6.4. Abbreviations of the components are defined as follows:

- $\text{Conv}(c_{in}, c_{out}, k, s, p)$: 2D convolution with c_{in} input channels, c_{out} output channels, kernel size k , stride s and padding p
- $\text{Deconv}(c_{in}, c_{out}, k, s, p)$: 2D deconvolution with c_{in} input channels, c_{out} output channels, kernel size k , stride s and padding p
- $\text{Upsample}(s)$: 2D nearest-neighbor upsampling with a scale factor s .
- $\text{GN}(n)$: group normalization [61] with n groups
- $\text{LReLU}(p)$: leaky ReLU [32] with a slope p

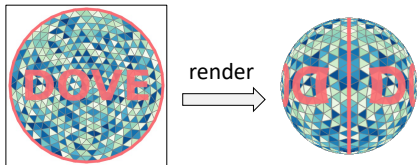
6.3 Training Details

The model is trained for 10 epochs, which takes three days on one NVIDIA RTX-6000 GPU. For each epoch, we iterate through the training set by densely sampling 8 short sequences in a batch for each iteration. The number of iterations in each epoch is therefore roughly the total number of frames in the training set, which is approximately 170k. Each sequence contains 8 consecutive frames.

During the first epoch, we disable instance-specific deformation and frame-specific articulation, and train the category-specific prior shape together with texture and rigid pose, in order to learn a prior shape over the entire category as well as rough texture and rigid pose estimations. After the second epoch, we decrease the weights of the shape regularizers to $1/5$, in order for the model to refine the

Table 3: Architecture of the shape f_S and pose network f_P . The network follows a convolutional encoder structure. n is the number of parameters predicted by each network.

Encoder	Output size
Conv(3, 64, 4, 2, 1) + LReLU(0.2)	64×64
Conv(64, 128, 4, 2, 1) + LReLU(0.2)	32×32
Conv(128, 256, 4, 2, 1) + LReLU(0.2)	16×16
Conv(256, 512, 4, 2, 1) + LReLU(0.2)	8×8
Conv(512, 512, 4, 2, 1) + LReLU(0.2)	4×4
Conv(512, 128, 4, 1, 0) + ReLU	1×1
Conv(128, n , 1, 1, 0) \rightarrow output	1×1



texture map (right half) initial sphere
 Figure 6: **Texture Mapping.** The texture is mapped from a circle in the texture to both, left and right side, of the initial sphere.

Table 4: Training details and hyper-parameter settings.

Parameter	Value/Range
Optimizer	Adam
Learning rate (f_S, f_P, f_T)	1×10^{-4}
Learning rate (ΔV_{ref})	1×10^{-2}
Number of iterations	170k
Number of sequences per batch	8
Number of frames per sequence	8
Loss weight λ_m	2
Loss weight λ_{dt}	0.5
Loss weight λ_{ins}	20
Loss weight λ_{Lap}	0.5
Loss weight λ_{nrm}	0.5
Loss weight λ_{flow}	100
Loss weight λ_{sym}	0.05
Input image size	128×128
Texture image size	128×128
Field of view (FOV)	25°
Camera location	(0, 0, 10)
Initial mesh center	(0, 0, 0)
Elevation angles	$(-90^\circ, 90^\circ)$
Azimuth angles	$(-180^\circ, 180^\circ)$
Number of bones	6

shape details. To better enforce temporal consistency, we randomly replace both the instance-specific shape and texture with the predictions averaged across the training sequence with a 50% probability.

We use Adam optimizers with a learning rate of 0.0001 for the networks and 0.01 for the trainable category shape parameters. The learning rates are decayed by a factor of 0.7 after each epoch starting from the third epoch (after the full deformable model is trained for one epoch).

6.4 Additional Results

Please refer to the **supplementary video** at dove3d.github.io for more qualitative results.

Shape Reconstruction Evaluation. As in Table 2 of the main paper, we evaluate the shape reconstruction quality and temporal consistency by re-projecting the shape of an object at frame t_0 to a future pose at frame $t_0 + \Delta t$. Figure 7 plots the mean Intersection over Union (mIoU) between the shape reprojections and the pseudo ground truth masks for various Δt . As the objects move over time, this estimates the consistency of the shape reconstructions across multiple views. We find that our model with articulation is able to correctly model the shape and deformation of the object over time. Moreover, the performance improvement gained by transferring the articulations also shows our model learns correct frame-specific articulations.

PCA Analysis on Learned Articulation Space. We analyze the learned articulated shape space using Principal Component Analysis (PCA). Figure 8 visualizes the first 6 principal components. The model learns meaningful articulations capturing typical bird movements.

Additional Reconstruction Results. Fig. 9 shows more bird reconstructions from various viewpoints. The model is robust against various input images, including frontal views and blurry images.

Texture Swapping and Animation. Our model reconstructs the birds in the canonical pose, where the shape and texture of different birds are aligned in the canonical representation. This allows us to easily edit the texture, for example swapping the texture with another bird, as shown in Fig. 10.

Moreover, with the learned articulation model, we can also easily animate the reconstructed birds in 3D, by rotating the bones, also illustrated Fig. 10.

Additional Qualitative Comparison. Fig. 11 provides a few more examples comparing the reconstruction results of our model and several state-of-the-art methods. Our model learns more accurate 3D shapes, despite not requiring explicit geometric supervision from keypoints, viewpoint or template shapes. More comparisons on entire video sequences are provided in the supplementary video.

Table 5: Architecture of the texture network f_T . The network follows an encoder-decoder structure.

Encoder	Output size
Conv(3, 64, 4, 2, 1) + GN(16) + LReLU(0.2)	64×64
Conv(64, 128, 4, 2, 1) + GN(32) + LReLU(0.2)	32×32
Conv(128, 256, 4, 2, 1) + GN(64) + LReLU(0.2)	16×16
Conv(256, 512, 4, 2, 1) + LReLU(0.2)	8×8
Conv(512, 512, 4, 2, 1) + LReLU(0.2)	4×4
Conv(512, 512, 4, 1, 0) + ReLU	1×1
Decoder	Output size
Deconv(512, 512, 4, 1, 0) + ReLU	4×4
Upsample(2) + Conv(512, 512, 3, 1, 1) + GN(128) + ReLU	8×8
Upsample(2) + Conv(512, 256, 3, 1, 1) + GN(64) + ReLU	16×16
Upsample(2) + Conv(256, 128, 3, 1, 1) + GN(32) + ReLU	32×32
Upsample(2) + Conv(128, 64, 3, 1, 1) + GN(16) + ReLU	64×64
Upsample(2) + Conv(64, 64, 3, 1, 1) + GN(16) + ReLU	128×128
Conv(64, 3, 5, 1, 2) + Sigmoid \rightarrow output T	128×128

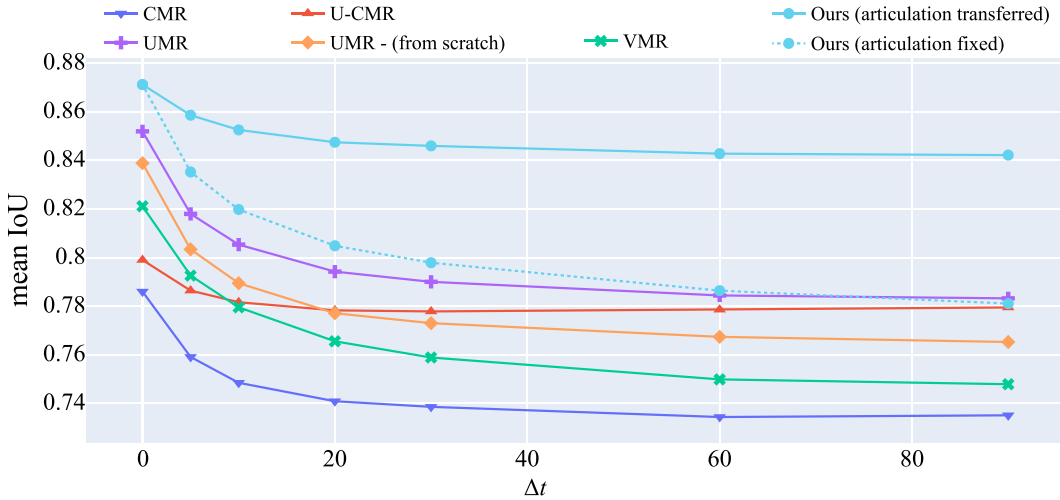


Figure 7: **Mask Reprojection IoU.** We project the shape predicted on frame t_0 to the pose predicted from a future frame $t_0 + \Delta t$ and measure the IoU with the ground truth mask at $t_0 + \Delta t$. Our method produces accurate shapes that are correctly projected to various poses in different frames, whereas others methods produce incorrect shapes indicated by significantly lower mask reprojection IoUs.

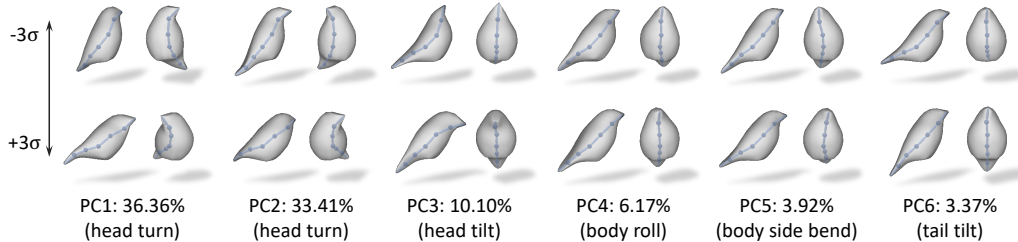


Figure 8: **PCA on Learned Articulations.** Our model learns meaningful articulations with the bone-based skinning model, including typical head and tail movements of birds.



Figure 9: **Additional Results.** We show the reconstructed birds from various viewpoints.

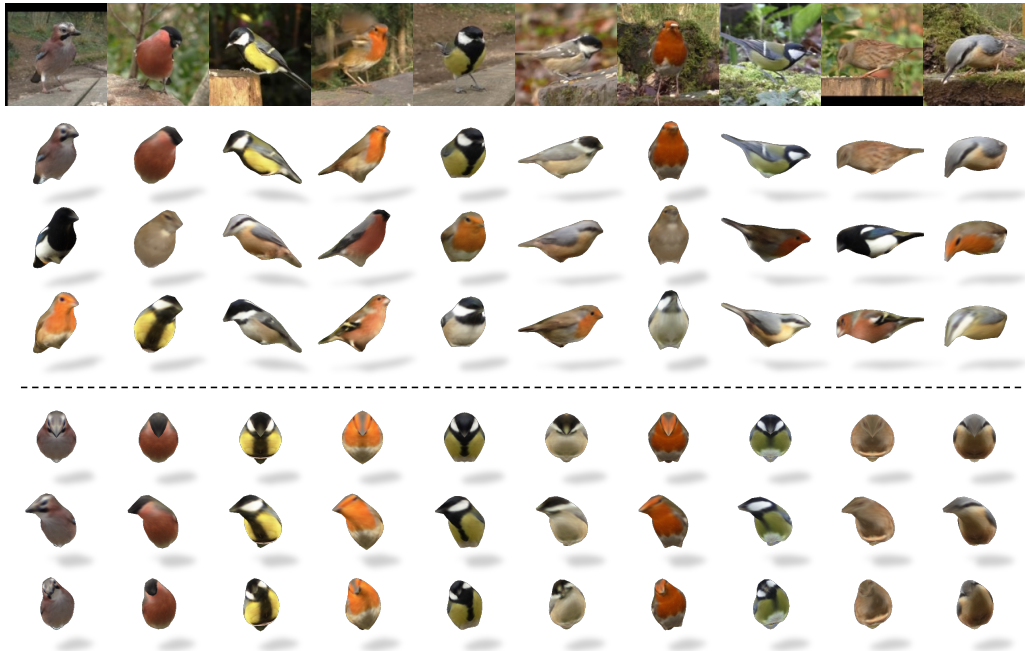


Figure 10: **Texture Swapping and Animation.** Top: since our model learns a canonical representation for all objects, we can easily swap the texture across different instances. Bottom: we can also easily animate the 3D birds using our learned articulation model.

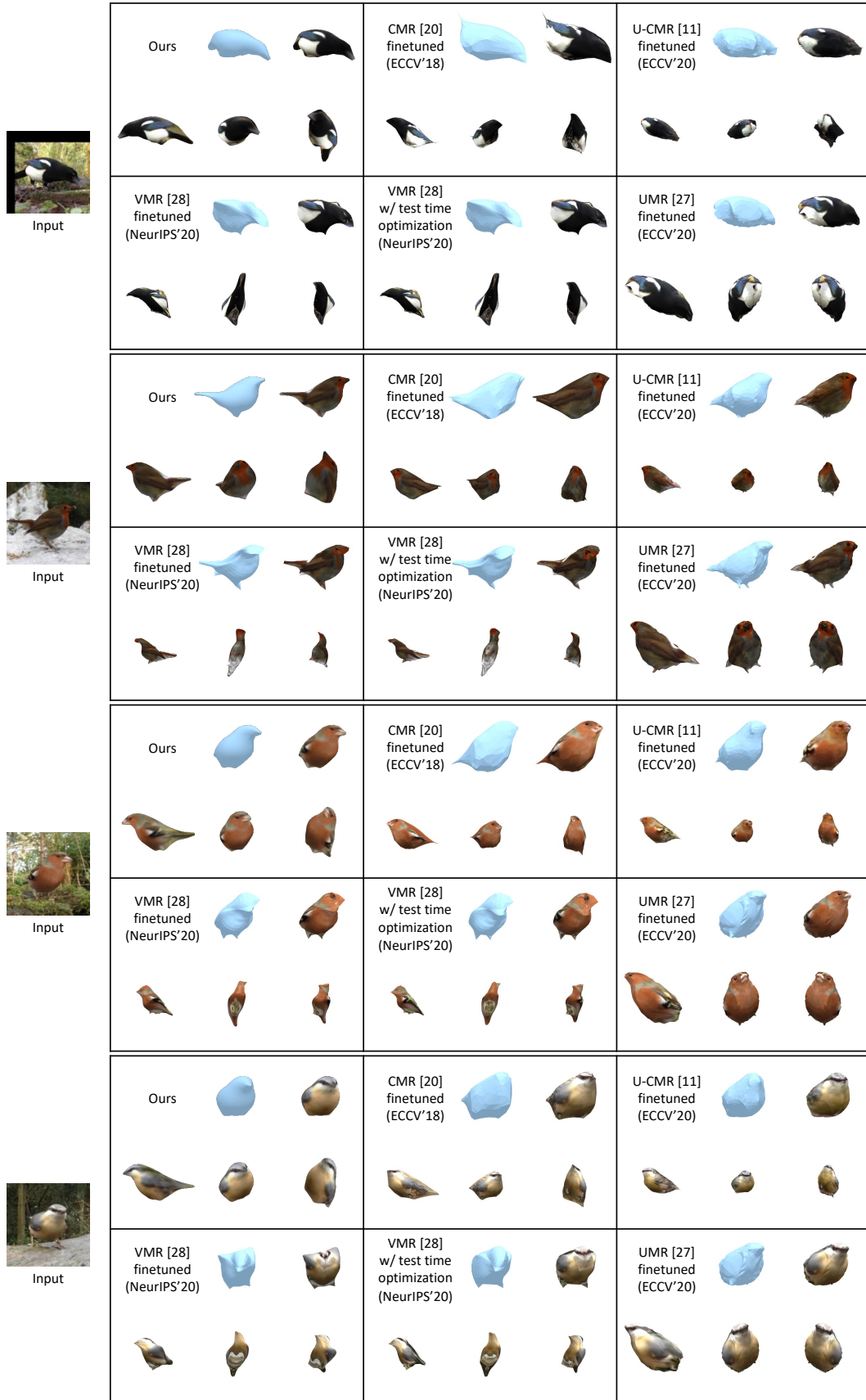


Figure 11: **Comparisons.** Our model learns more plausible 3D shapes compared to SOTA methods.